Aerosol and Air Quality Research, x: 1–9, xxxx

ISSN: 1680-8584 print / 2071-1409 online
doi: 10.4209/aaqr.2017.10.0385

Statistical Comparison of Regional-Scale Tropospheric Aerosol Extinction Coefficient across China Based on CALIPSO Data

Yujun Qiu[1*], Leiming Zhang[2], Yongsheng Chen[3]

[1] *School of Atmospheric Physics, Nanjing University of Information Science and Technology, Nanjing 210044, China*
[2] *Air Quality Research Division, Environment and Climate Change Canada, Toronto, ON M3H 5T4, Canada*
[3] *Department of Atmospheric Science, York University, Toronto, ON M3J 1P3, Canada*

ABSTRACT

Two years of CALIPSO level 2 version 2 data were analyzed to obtain regional distributions of vertical profiles of the aerosol extinction coefficient (AEC) across China. 10 typical geographical regions were selected for comparison, which cover various aerosol pollution levels, climate zones, and underlying surfaces. The whole troposphere was split into two-layers: the Lower- and the Upper-layer—separated by the maximum boundary layer height—which represent the boundary layer and the upper tropospheric layer, respectively. The annual average of the column-average AEC in the 10 regions ranged from 0.066 to 0.243 km^{-1} in the Lower-layer and from 0.022 to 0.059 km^{-1} in the Upper-layer. The regional AEC in the Lower-layer was the highest in central and eastern China, followed by that in the Sichuan Basin, the Yunnan-Guizhou Plateau, the capital economic circle, the Pearl River Delta, the desert region, the Tibetan Plateau, northeast China, the northwest semi-arid plateau, and, finally, the East China Sea. The seasonal AEC in the Lower-layer was the highest during spring in the desert and marine regions, during the summer on the Tibetan Plateau, and during autumn or winter in the other regions. The regional and seasonal patterns of AEC in the Lower-layer agreed to a large extent with known regional distributions of surface-layer $PM_{2.5}$ distributions and dominant seasonal emission sources in their respective regions. Regional and seasonal patterns in the Upper-layer were slightly different from those in the Lower-layer due to different transport pathways of aerosol pollution in different regions. The proportion of occurrence under different pollution conditions and the number of polluted days were also estimated separately for the Lower- and the Upper-layer, based on AEC vertical profiles for each region.

Keywords: Tropospheric aerosol; Aerosol pollution; Aerosol column average; Occurrence frequency.

INTRODUCTION

Knowledge of spatial and temporal distributions of tropospheric aerosols is needed in order to address their impacts on air quality and climate related issues (Menon *et al.*, 2002; Lelieveld *et al.*, 2002; Watson, 2002, Li, *et al.*, 2011; Ma *et al.*, 2014; Sheng *et al.*, 2016). The globally increasing atmospheric aerosol loading has added large uncertainties in regional and global climate models used for addressing aerosol-cloud integration and aerosol climate effects due to the difficulties in quantifying aerosol spatial distributions and their radiative properties (Knippertz *et al.*, 2015; Seinfeld *et al.*, 2016). Aerosol optical properties measured by satellites can fill some of the knowledge gaps (Winker *et al.*, 2007; Martin *et al.*, 2008). For example, data collected by the Moderate Resolution Imaging Spectroradiometer (MODIS) have been used to provide column-integrated aerosol optical properties covering regional to global scales (Kim *et al.*, 2007; Kosmopoulos *et al.*, 2008; Zhang *et al.*, 2010) and estimate ground-level $PM_{2.5}$ and PM_{10} in various regions of the world (van Donkelaar *et al.*, 2006; Zhang *et al.*, 2010; He *et al.*, 2012; Zheng *et al.*, 2013).

Compared to MODIS data, the Cloud-Aerosol Lidar and Infrared Pathfinder Satellite Observation (CALIPSO) provide continuous aerosol profiling covering multiple vertical layers globally, which provides an unprecedented opportunity for advancing the understanding of aerosol distribution characteristics on large-scales (Winker *et al.*, 2007, 2010). Example applications of CALIPSO data include investigating seasonal variations of aerosol vertical distribution globally (Yu *et al.*, 2010; Huang *et al.*, 2013), analyzing annual and seasonal patterns of the aerosol extinction coefficient (AEC) over 13 sub-continental regions representative of industrial, dust, and biomass burning pollution sources (Koffi *et al.*, 2012), identifying an aerosol layer at the tropopause level

* Corresponding author.
Tel.: +86-13770853075; Fax: +86-02558699771
E-mail address: qyj@nuist.edu.cn

associated with the Asian monsoon (Vernier *et al.*, 2011), and providing vertical profiles of aerosols and AEC in various regions (Campbell *et al.*, 2013; Ma *et al.*, 2014).

China is among the most polluted regions in the world due to its economy booming in the past three decades (Zhang *et al.*, 2012; Han *et al.*, 2014; Sheng *et al.*, 2016). Measurements of aerosol chemical and optical properties were mostly made at limited surface stations (Yu *et al.*, 2013; Sun *et al.*, 2015; Tao *et al.*, 2017). Several studies have used remote sensing data for quantifying aerosol distributions across China (He *et al.*, 2012; Zheng *et al.*, 2013; Sun and Chen, 2017; Xiao *et al.*, 2017; Yu *et al.*, 2017). However, little effort has been made to investigate the vertical distribution characteristics of atmospheric aerosols. The present study aims to characterize regional distribution patterns of atmospheric aerosols at both lower- and upper-layers of the troposphere across China through analyzing aerosol AEC data provided by the CALIPSO Lidar observations. Knowledge gained in this study can be used for improving climate models and for making future emission control policies.

METHODOLOGY

Selected Regions

Based on geographical location and dominant underlying surface type, 10 regions (R1–R10) in China were defined and selected for the comparison of aerosol extinct coefficient profiles and probability distributions. Fig. 1 shows the locations of the 10 regions, and Table SI-1 in the Supplementary Information (SI) document lists their boundary latitude and longitude values. R1 covers most areas of the Taklimakan desert area; R2 is inside the northwest part of the semi-arid plateau covering part of Gobi sand and Loess Plateau areas; R3 is the Beijing-Tianjin-Hebei region (the capital economic circle); R4 covers most of the northeast China, a major agricultural zone with plenty of plains and forests; R5 covers most of the Tibetan Plateau; R6 covers the whole Sichuan Basin and surrounding areas; R7 is in the middle part of central and eastern China, with dense population, and covers the Yangtze River Delta region; R8 mainly covers the Yunnan-Guizhou Plateau; R9 is in the southern coastal area of China and covers the Pearl River Delta economic region as well as Fujian Province; and R10 is inside the East Sea of China. These regions cover different economic belts, climate zones, topography, and pollution levels in China.

Satellite Data

The Cloud-Aerosol Lidar with a Orthogonal Polarization (CALIOP) instrument installed on the CALIPSO satellite measures vertical profiles of elastic backscatter at 532 and 1064 nm near nadir during both day and night phases of the orbit. The backscatter coefficient data were converted to aerosol and cloud properties, including the aerosol extinction coefficient (AEC) and aerosol optical depth (AOD). High spatial resolution continuous measurements of vertical profiles of aerosol and cloud optical properties globally have been available since mid-June of 2006 (Winker *et al.*, 2007, 2009). AEC data at the 532 nm wavelength from June 2006 till September 2008 were analyzed in the present study. Level 2 aerosol profile data at 5 km horizontal resolution covering the 10 regions of China defined above were extracted for all the vertical levels. Table SI-2 in the SI document provides the numbers of samples of the AECs during the four seasons in the 10 regions.

Data Analysis

To explore the contribution of AEC in different value ranges to the average value of AEC in any given region and season, the whole AEC range (0.0–1.25 km^{-1}) was divided into 10 equal intervals, i.e., the first interval is from 0 to 0.125 km^{-1}; the second one, from 0.125 to 0.250 km^{-1};

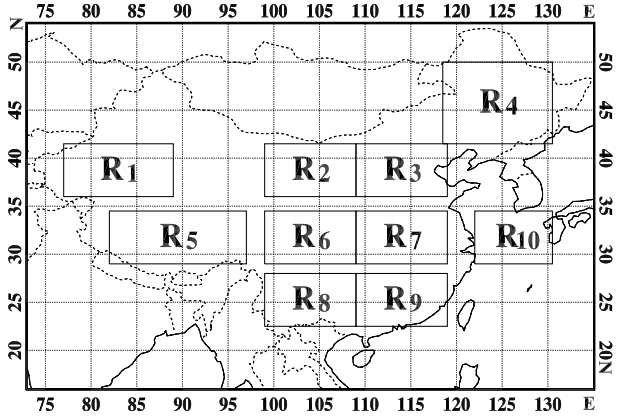

Fig. 1. Selected regions in China: R1 is referred to Taklamakan desert area; R2, Gobi sand and Loess Plateau areas; R3, the Capital economic circle; R4, Northeast China; R5, Tibet Plateau; R6, Sichuan Basin; R7, Yangtze River Delta; R8, Yunnan-Guizhou Plateau; R9, mainly Pearl River Delta economic region; and R10, East China Sea.

and so on; and the tenth one, from 1.125 to 1.25 km^{-1}. The first interval of AEC should represent the cleanest condition and the last one, the most heavily polluted condition in terms of aerosol concentration. Based on China's Air Quality Index (AQI) (HJ633-2012), aerosol pollution can be roughly categorized into three levels: clean, light- polluted, and heavy-polluted, corresponding to AQIs of < 100, 100–200, and > 200, or $PM_{2.5}$ concentrations of < 75, 75–150, and > 150 μg m^{-3}, respectively. AEC values corresponding to these $PM_{2.5}$ concentration cutting points will vary with aerosol chemical composition, among other factors. Based on values found in Tao *et al.* (2015) for different pollution conditions in Beijing, we can assume the first and second AEC intervals as clean conditions, the next four intervals as light-polluted conditions, and the last four intervals as heavy-polluted conditions.

For statistical comparison between the 10 different regions, column-integrated values, rather than data at selected heights, were used for analysis to minimize the uncertainties inherited from the measurement. Considering that aerosol concentration varies greatly with height and so does the AEC value, AEC data were compared separately for two layers: One is from 60 m high to the top of the boundary layer height (BLH) (referred to as the Lower-layer), and the other is from BLH to 8 km (referred to as the Upper-layer). AEC data at a height of 0–60 m (the lowest layer detected by the satellite) were excluded from Lower-layer analysis due to the large uncertainties caused by surface reflectivity, while data from 8 km high were excluded from Upper-layer analysis due to the contributions of cirrus clouds to AEC. Although the AEC data were supposed to have removed the contributions from clouds, the impact of cirrus clouds to AEC could not be excluded completely by the CALIOP instrument due to the very thin layers of such clouds and their weak contributions to AEC (Omar *et al.*, 2013). Note that the Lower-layer represents the whole boundary layer, while the Upper-layer represents the upper troposphere.

BLH changes with time and location, and average BLH can be determined from the vertical profiles of AEC, i.e., at the height where the maximum variance of the AEC appears (Stull and Eloranta, 1984; Menut *et al.*, 1999; Lammert *et al.*, 2006; Emeis *et al.*, 2008; Luo *et al.*, 2014a). CALIPSO provides lidar data for retrieving BLH globally (Jordan *et al.*, 2010; McGrath-Spangler and Denning, 2013; Zhang *et al.*, 2016). The present study, however, developed a method for extracting the maximum BLH for any given region (R1–R10) and during any given season (spring [March–May], summer [June–August], autumn [September–November], and winter [December–February]) using the approach described below. In the first step, the probability of each AEC interval appearing at every height was calculated as the ratio of the number of AECs in the selected AEC interval and height to the total number of AECs for all AEC intervals within the whole column on a seasonal basis. In the second step, vertical profiles of AEC probability were plotted for all the AEC intervals, and BLH for each AEC interval was identified based on the maximum variance of the AEC probability, as mentioned above (Fig. SI-1). A linear regression between BLH and AEC interval was then plotted, and the interception of BLH (with AEC = 0) was defined as the maximum BLH (see a linear regression for R1 and R2 in spring in Fig. SI-2(a) as an example). The seasonal maximum BLH was used to separate Lower-layer and Upper-layer defined above for AEC analysis. The seasonal maximum BLH was found to be as low as 0.5 km in region R10 and as high as 3 km in R5 and R8, which was consistent with their respective underlying surfaces or terrains (e.g., ocean in R10 and plateau in R5 and R8).

RESULTS

Overview of AEC Vertical Profiles

The annual average AEC decreased from the surface with increasing height and reached the minimum values at an altitude around 8–9 km. AEC at the surface ranged from 0.05 to 0.32 km^{-1}, depending on the region, and ranged from 0.012 to 0.022 km^{-1} at an altitude of 8–9 km (Fig. 2). The vertical variabilities of the annual average AEC within the Lower-layer were in the range of 0.127–0.060, 0.082–0.051, 0.269–0.084, 0.095–0.062, 0.356–0.025, 0.288–0.173, 0.286–0.170, 0.323–0.094, 0.194–0.072, and 0.071–0.045 km^{-1} for regions R1 to R10, respectively. The vertical variabilities of the annual average AEC within the Upper-layer were in the range of 0.104–0.013, 0.069–0.012, 0.081–0.017, 0.070–0.015, 0.039–0.010, 0.165–0.013, 0.163–0.021, 0.091–0.021, 0.130–0.023, and 0.070–0.020 km^{-1} for regions R1 to R10, respectively. Regional differences in the probability profiles associated with different pollution levels (clean, light-polluted, and heavy-polluted) are very large (Fig. 3), with the maximum probability appearing at different heights in different regions, likely dominated by different aerosol sources and BLH values. Seasonal differences in the average AEC profiles were significant in some regions (e.g., R1, R3, R4, R8), especially in the Lower-layer (Fig. SI-3). Considering the large differences in AEC between the Lower-layer and Upper-layer, the column-averaged AEC and probability are discussed separately below on an annual and seasonal basis. All values mentioned in the following sections refer to regional- as well as column-averaged values unless specified differently.

Regional AEC in the Lower-layer

Annual AEC

The annual average AEC for the Lower-layer showed regional differences up to a factor of 3.7 (ranging from 0.066 to 0.243 km^{-1}) and in the sequence of R7, R6, R8, R3, R9, R1, R5, R4, R2, and R10 from the largest to the smallest. The lowest AEC in R10, among all the regions, was apparently due to the minimum aerosol loading over marine surfaces. The highest AECs were mostly found in industrial areas with high population densities, such as the Yangtze River delta (R7), Sichuan Basin (R6), capital economic circle (R3), and Pearl River Delta (R9). Surface-level $PM_{2.5}$ concentrations in these regions were consistently higher than in most of the other regions. For example, Tao *et al.* (2017) showed the annual $PM_{2.5}$ from available measurements to be 115 μg m^{-3} in the capital economic circle,

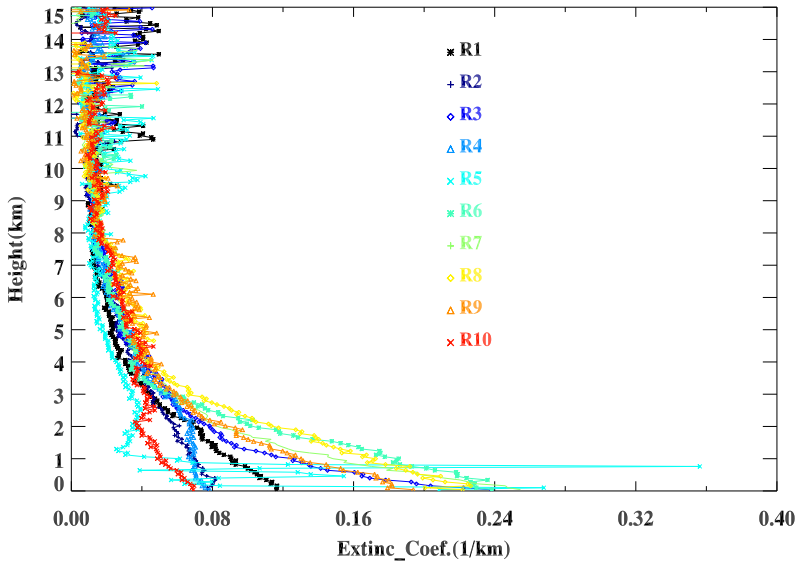

Fig. 2. Vertical profiles of annual average extinction coefficient (AEC) in the 10 regions based on the CALIPSO level 2 lidar data.

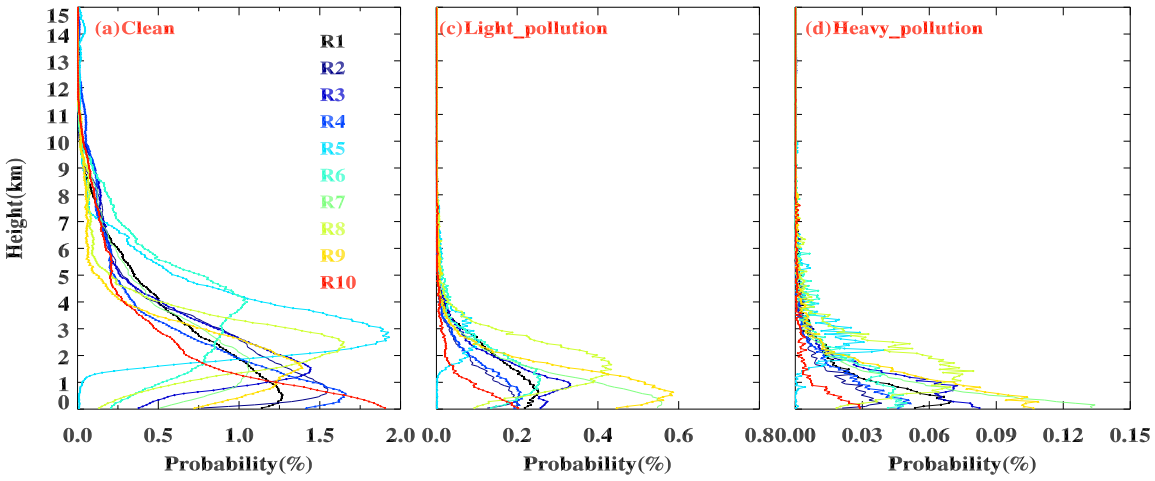

Fig. 3. Annual average vertical profiles of probability of occurrence for clean, light-polluted, and heavy-polluted conditions in the 10 regions.

100 μg m^{-3} in the Sichuan Basin, 148.9 μg m^{-3} in central and eastern China, and 76.8 μg m^{-3} in the Pearl River Delta economic region. It is noted that the Yunnan-Guizhou Plateau (R8) was also among the regions with the highest AEC; however, no $PM_{2.5}$ measurements were available in this region for a direct comparison with the other regions. $PM_{2.5}$ levels were suspected to be at high levels due to the establishment of a large number of coal-mining factories since the 1990s (Zheng *et al.*, 2010). Decreasing trends in sunshine duration from the 1990s till 2005 have been observed in this as well as other regions of China, likely due to the increased aerosol loading (Kaiser *et al.*, 2002; Zheng *et al.*, 2008). It is further noted that BLH in R8 was higher than in the other regions (Fig. SI-2), and the maximum AEC probability for polluted conditions reached 2 km in this region while being below 1.5 km in most of the other regions (Fig. SI-1). This is likely another reason for the high AEC in R8 in the Lower-layer. The regional distribution of AEC presented above was mostly consistent with that of aerosol optical depth based on the 10 years of MODIS remote sensing data (Luo *et al.*, 2014b).

The proportion of occurrence (POC) in the 10 regions was in the range of 48.1–92.9%, 5.5–42.1% and 1.3–9.8% for clean, light-polluted and heavy-polluted conditions, respectively, on an annual basis (Table 2). POC was calculated for the whole Lower-layer (or Upper-layer) by

Table 2. The probability of occurrence (POC) for clean, light polluted and heavy polluted conditions in the Lower-layer and Upper-layer over the 10 regions. POC was calculated for the whole Lower-layer (or Upper-layer) by adding all the cases together covering various altitudes on seasonal and annual basis.

		R1	R2	R3	R4	R5	R6	R7	R8	R9	R10
Lower-layer											
Clean	Annual	80.8	86.2	71.7	85.2	92.9	58.1	48.1	69.3	60.7	90.0
	Spring	62.4	86.5	81.2	83.1	97.6	60.1	64.4	69.6	70.5	86.2
	Summer	78.0	83.5	65.7	83.2	86.7	57.8	46.6	71.4	67.2	93.6
	Autumn	87.6	91.3	68.4	88.1	87.6	62.9	44.9	60.8	53.4	91.5
	Winter	87.8	82.2	72.8	85.3	96.1	48.2	42.6	76.3	55.4	85.5
Light polluted	Annual	15.5	11.8	22.7	12.1	5.5	34.5	42.1	26.1	33.0	8.7
	Spring	28.5	11.2	16.3	13.5	1.8	33.4	30.6	25.4	24.9	12.3
	Summer	17.5	13.6	26.1	13.1	10.4	35.2	41.5	24.5	27.6	5.3
	Autumn	10.2	7.5	24.9	10.1	9.2	30.6	44.5	33.6	39.2	7.9
	Winter	11.1	15.6	22.4	12.3	3.0	41.3	47.1	19.9	37.2	12.2
Heavy polluted	Annual	3.7	2.1	5.6	2.7	1.7	7.3	9.8	4.6	6.3	1.3
	Spring	9.0	2.3	2.4	3.3	0.6	6.5	4.9	5.0	4.6	1.6
	Summer	4.4	2.9	8.3	3.7	2.8	7.0	11.9	4.0	5.2	1.1
	Autumn	2.2	1.2	6.6	1.9	3.2	6.5	10.6	5.6	7.4	0.7
	Winter	1.2	2.2	4.8	2.4	0.9	10.5	10.3	3.8	7.3	2.4
Upper-layer											
Clean	Annual	90.0	94.3	93.3	91.6	96.0	91.0	86.2	89.5	84.0	93.9
	Spring	85.8	96.2	96.1	91.3	99.1	93.8	91.1	91.4	86.1	93.5
	Summer	89.4	92.5	90.4	90.1	92.8	85.3	82.4	85.4	79.9	94.5
	Autumn	93.1	95.4	93.8	94.2	88.8	90.7	82.3	87.4	79.5	94.5
	Winter	96.9	93.1	93.9	91.8	98.9	96.3	88.3	93.8	90.7	93.2
Light polluted	Annual	9.0	5.0	6.0	7.3	3.3	7.9	12.3	9.1	14.2	5.4
	Spring	12.7	3.4	3.5	7.5	0.7	5.4	8.1	7.5	12.4	5.9
	Summer	9.6	6.5	8.5	8.8	5.9	13.1	15.3	12.6	17.9	4.7
	Autumn	6.2	3.9	5.7	5.0	9.3	7.8	15.6	10.9	18.1	5.1
	Winter	2.8	6.1	5.4	7.2	1.0	3.3	10.8	5.5	8.3	5.7
Heavy polluted	Annual	1.0	0.7	0.7	1.1	0.7	1.1	1.5	1.4	1.8	0.7
	Spring	1.5	0.4	0.4	1.2	0.2	0.9	0.9	1.0	1.6	0.5
	Summer	1.0	0.9	1.1	1.2	1.2	1.6	2.4	2.1	2.2	0.7
	Autumn	0.8	0.7	0.5	0.9	1.8	1.5	2.1	1.8	2.3	0.4
	Winter	0.3	0.7	0.7	1.1	0.1	0.4	1.0	0.8	1.0	1.1

adding all the cases together, covering various altitudes on a seasonal and annual basis. R7, R6, and R9 were the top three regions for high POC for both heavy-polluted (6.3–9.8%) and light-polluted (33–42.1%) conditions, followed by R3 and R8. R5 and R10 were the only two regions with POC values lower than 2% for heavy polluted and lower than 10% for light-polluted conditions. While in general, regions having high $PM_{2.5}$ concentrations and/or high AEC also had high POC for heavy- and light-polluted conditions, there were some inconsistences between the regions in terms of their orders of the highest to lowest values (e.g., R3 and R8), which were likely caused by other factors such as different aerosol chemical compositions and meteorological conditions in different regions (Tao *et al.*, 2017).

The numbers of days with light- and heavy-polluted conditions were also estimated based on the vertical profiles of AEC POC (Table 3). Note that if at any height within the Lower-layer AEC followed into the 3rd–6th (7th–10th) intervals, it was treated as light-polluted (heavy-polluted). On an annual basis, R7, R8, and R9 were the top three regions with the most light-polluted (90–113) and heavy polluted (15–22) days. R3 (the capital economic circle) only had 62 light-polluted days and 13 heavy-polluted days. R5 (the Tibetan Plateau) and R10 (the East China Sea) had the lowest number of light- (20 and 43, respectively) and heavy-polluted (9 and 5, respectively) days. Again, the regional pattern of the number of polluted days was somewhat different from that of surface-layer $PM_{2.5}$ concentration. For example, R3 and R4 (in northern China) were expected to have as many polluted days as or even more than R7, R8, and R9, based on ground measurements of $PM_{2.5}$ concentrations. This implies that using AEC profile data may only allow us to semi-quantitatively identify $PM_{2.5}$ concentration levels in different regions due to the large variations in $PM_{2.5}$ chemical composition.

Seasonal AEC

The 10 regions studied here cover different climate zones, with very different seasonal meteorological conditions, which can influence pollutant sources, transport, chemical transformation, and atmospheric dry and wet removal processes. Besides, there are different dominant seasonal

Table 3. The estimated number of days under light- and heavy-polluted conditions in the Lower-layer and Upper-layer over the 10 regions on annual and seasonal basis. This is done by multiplying the 365 days with the maximum probability of EC vertical profile of the 10 individual EC intervals (the 3rd–6th intervals were summed as light-polluted and the 7th–10th intervals were summed as heavy polluted).

		R1	R2	R3	R4	R5	R6	R7	R8	R9	R10
Lower-layer											
Light polluted	Annual	53	41	62	47	20	53	96	90	113	43
	Spring	15	7	10	9	2	8	13	21	13	11
	Summer	15	11	17	14	10	24	25	24	32	8
	Autumn	10	9	17	11	5	11	25	28	41	13
	Winter	13	14	18	13	3	10	33	17	27	11
Heavy polluted	Annual	11	7	13	9	9	11	22	15	17	5
	Spring	4	2	1	2	2	2	2	3	2	1
	Summer	4	2	4	3	2	4	5	4	5	2
	Autumn	2	1	4	2	3	3	6	5	6	1
	Winter	1	2	4	2	2	2	9	3	4	1
Upper-layer											
Light polluted	Annual	44	32	39	41	24	50	83	58	96	42
	Spring	15	7	6	11	3	9	13	16	12	12
	Summer	16	11	16	17	11	26	23	19	34	8
	Autumn	9	6	11	8	8	9	23	18	39	13
	Winter	4	8	6	5	2	6	24	5	11	9
Heavy polluted	Annual	6	5	6	6	9	8	11	8	13	6
	Spring	3	1	1	1	2	2	1	2	2	1
	Summer	2	2	3	2	3	3	4	3	4	2
	Autumn	1	1	1	2	3	2	3	2	5	1
	Winter	0	1	1	1	1	1	3	1	2	2

emission sources in different regions, as summarized in Tao *et al.* (2017). To explore how the seasonal emission sources were reflected in AEC patterns, seasonally averaged AEC, POC, and the estimated number of polluted days were generated (Tables 2 and 3).

Seasonal variations in AEC were mostly in the range of 39%–73% in all the regions, except for reaching a factor of 3.4 in R5. The very high seasonal variation in R5 was mostly due to the high AEC value in summer. The highest seasonal average for AEC appeared in spring in R1 and R10, summer in R5, autumn in R3 and R8, and winter in R2, R4, R6, R7, and R9. The highest seasonal AEC in spring in R1 (desert region) and R10 (marine) was likely due to strong winds in this season lifting surface-level soil dust or sea-salt aerosols to upper levels. In contrast, the lowest seasonal average for AEC was found in spring in R3 (the capital economic region), likely due to the frequent strong winds from the western and northern mountains to the southern plains of the region, which were conducive to pollutant diffusion. Surface $PM_{2.5}$ concentrations observed in several major cities of this region (Beijing, Tianjin, and Shijiazhuang) averaged 138, 121, 155, and 186 μg m^{-3} in spring, summer, autumn, and winter, respectively (Tao *et al.*, 2017), which were mostly consistent with the seasonal AEC patterns. The highest seasonal AEC in autumn in R8 reflected the influence of extensive biomass burning activities in this region (Cao *et al.*, 2005). The highest seasonal AEC values in the other four regions in winter should be due to the residential fossil fuel and coal burning, as discussed in Tao *et al.* (2017).

Seasonal patterns of the number of light- and heavy-polluted days were also different from region to region. For example, there were more (light plus heavy) polluted days in spring and summer than in fall and winter (19 versus 12–14) in R1, least polluted days in spring (4–15) than in the other seasons (5–47) in R2, R3, R4, R5, R6, R7 and R9, most polluted days in summer (12–28) than in the other seasons (4–15) in R4, R5 and R6. Every season had a substantial number of polluted days (20–33) in R8.

Regional AEC in the Upper-layer

Annual AEC

The annual average for AEC for the Upper-layer showed regional differences up to a factor of 2.7 (ranging from 0.022 to 0.059 km^{-1}), which were smaller than those in the Lower-layer. The sequence from the largest to smallest (R9, R7, R1, R6, R8, R4, R3, R2, R10, and R5) was also very different from that in the Lower layer, suggesting different vertical transport patterns of aerosol pollution in different regions. For example, AEC in R1 ranked the third largest among all the regions in the Upper-layer but ranked sixth in the Lower-layer, which can be partially explained by dust transport patterns shown by Huang *et al.* (2008). The vertical distribution characteristics of dust aerosols in the Taklimakan Desert showed a two-layer structure with the highest dust frequencies appearing at 9–11 km and at 3 km. In contrast, AEC in R3 ranked only seventh in the Upper-layer but fourth in the Lower-layer, indicating inefficient vertical transportation as a result of efficient horizontal diffusion, as mentioned above.

Despite high altitudes, POC on an annual basis still reached 3.3%–14.2% and 0.7%–1.8% for light- and heavy-polluted conditions, respectively. The totals for light- and heavy-polluted days were estimated to be 33 to 109 days, depending on the region. POC for polluted conditions and the estimated number of polluted days were larger in the eastern and southern regions (R9, R7, and R8) than in the western and central regions (R1 and R6), northern regions (R4 and R3), East China Sea (R10), northwest region (R2), and Tibetan Plateau (R5). Such a regional pattern was similar to yet slightly different from that for AEC, as discussed above.

Seasonal AEC

Seasonal variations of regionally averaged AEC in the Upper-layer were in the range of 10%–58%—much smaller than those in the lower layer. The highest seasonal value occurred in summer in R1, R2, R3, R4, and R5 and in autumn in R6, R7, and R8. Seasonal variations in R9 and R10 were not significant (10% and 16%, respectively). Seasonal POC for polluted conditions were the largest in summer or autumn in all regions except desert and ocean regions. The number of light- and heavy-polluted days were on the order of 20 days in summer or autumn with many fewer in spring and winter. The larger values of AEC and POC in warm seasons were likely due to stronger convection, which transported more pollutants to high altitudes.

CONCLUSIONS

Regional and seasonal AECs in the boundary layer and upper troposphere were quantified for 10 typical geographical regions in China. Regional variations in the annual average AEC were up by a factor of 3.7 in the Lower-layer and a factor of 2.7 in the Upper-layer. Seasonal variations in AEC within each region were mostly on the order of a few dozen percent. The proportion of occurrence (POC) under clean, light-polluted and heavy-polluted conditions was also calculated based on the vertical profiles of AEC distributions. On an annual basis, POC in the Lower-layer ranged from 5.5% to 42.1% and from 1.3% to 9.8%, depending on the region, for light- and heavy-polluted conditions, respectively. POC in the Upper-layer still reached above 10% in some regions. Depending on the region, on an annual basis, the number of light-polluted days was estimated to be in the range of 20–113 and the number of heavy-polluted days, in the range of 5–22 days in the Lower-layer, with corresponding numbers of 24–96 and 5–13 in the Upper-layer.

This study provides an AEC database that can be used to evaluate climate models and guide future measurement needs in aerosol pollution. For example, the Yunnan-Guizhou Plateau was found to have AEC values similar to those in the most polluted regions of central and northern China; these results need to be verified by field measurements of chemically resolved $PM_{2.5}$ data. There are also some discrepancies between the AEC values, the estimated number of polluted days and the limited surface-level $PM_{2.5}$ data in terms of regional distributions, which may be explained by air-quality model simulations. The boundary-layer height generated in this study also needs to be verified in future studies, which may in turn improve the method developed here.

ACKNOWLEDGEMENTS

We greatly appreciate the NASA CLIPASO Data Processing Center for providing data used in the present study. This study was funded by the National Natural Science Foundation of China (Grant numbers: 41475035 and 91544109).

SUPPLEMENTARY MATERIAL

Supplementary data associated with this article can be found in the online version at http://www.aaqr.org.

REFERENCE

Campbell, J.R., Reid, J.S., Westphal, D.L., Zhang, J., Tackett, J.L., Chew, B.N., Welton, E.J., Shimizu, A., Sugimoto, N., Aoki, K. and Winker, D.M. (2013). Characterizing the vertical profile of aerosol particle extinction and linear depolarization over Southeast Asia and the Maritime Continent: The 2007-2009 view from CALIOP. *Atmos. Res*. 122: 520–543.

Cao, G.L., Zhang, X.Y., Wang, D. and Zheng, F.C. (2005). Inventory of atmospheric pollutants discharged from biomass burning in China continent. *China Environ. Sci.* 25: 389–393.

Emeis, S., Schafer, K. and Munkel, C. (2008). Surface-based Remote Sensing of the Mixing-layer Heigh-A Review. *Meteorol. Z.* 17: 621–630.

Han, L., Zhou, W., Li, W. and Li, L. (2014). Impact of urbanization level on urban air quality: A case of fine particles ($PM_{2.5}$) in Chinese cities. *Environ. Pollut*. 194: 163–170.

He, Q., Li, C., Geng, F., Lei, Y. and Li, Y. (2012). Study on long-term aerosol distribution over the land of East China using MODIS data. *Aerosol Air Qual. Res.* 12: 304–319.

Huang, J., Minnis, P., Chen, B., Huang, Z., Liu, Z., Zhao, Q., Yi, Y. and Ayers, J.K. (2008). Long-range transport and vertical structure of Asian dust from CALIPSO and surface measurements during PACDEX. *J. Geophys. Res.* 113: D23212.

Huang, L., Jiang, J.H., Tackett, J.L., Su, H. and Fu, R. (2013). Seasonal and diurnal variations of aerosol extinction profile and type distribution from CALIPSO 5-year observations. *J. Geophys. Res*. 118: 4572–4596.

Jordan, N.S., Hoff, R.M and Bacmeister, J.T. (2010). Validation of Goddard Earth Observing System-version 5 MERRA planetary boundary layer heights using CALIPSO. *J. Geophys. Res*. 115: D24218.

Kaiser, D.P. and Y. Qian. (2002). Decreasing trends in sunshine duration over China for 1954-1998: Indication of increased haze pollution? *Geophys. Res. Lett*. 29: 2042.

Kim, S.W., Yoon, S.C., Kim, J. and Kim, S.Y. (2007).

Seasonal and monthly variations of columnar aerosol optical properties over east Asia determined from multi-year MODIS, LIDAR, and AERONET Sun/sky radiometer measurements. *Atmos. Environ.* 41: 1634–1651.

Knippertz, P., Evans, M.J., Field, P.R., Fink, A.H., Liousse, C. and Marsham, J.H. (2015). The possible role of local air pollution in climate change in West Africa. *Nat. Clim. Change* 5: 815–822.

Koffi, B., Schulz, M., Bréon, F., Griesfeller, J., Winker, D., Balkanski, Y., Bauer, S., Berntsen, T., Chin, M., Collins, W.D., Dentener, F., Diehl, T., Easter, R., Ghan, S., Ginoux, P., Gong, S., Horowitz, L.W., Iversen, T., Kirkevåg, A., Koch, D., Krol, M., Myhre, G., Stier, P. and Takemura, T. (2012). Application of the CALIOP layer product to evaluate the vertical distribution of aerosols estimated by global models: AeroCom phase I results. *J. Geophys. Res*. 117: D10201.

Kosmopoulos, P.G., Kaskaoutis, D.G., Nastos, P.T., and Kambezidis, H.D. (2008). Seasonal variation of columnar aerosol optical properties over Athens, Greece, based on MODIS data. *Remote Sens. Environ.* 112: 2354–2366.

Lammert, A. and Bösenberg, J. (2006). Determination of the convective boundary-layer height with laser remote sensing. *Boundary Layer Meteorol.* 119: 159–170.

Lelieveld, J., Berresheim, H., Borrmann, S., Crutzen, P.J., Dentener, F.J., Fischer, H., Feichter, J., Flatau, P.J., Heland, J., Holzinger, R., Korrmann, R., Lawrence, M.G., Levin, Z., Markowicz, K.M., Mihalopoulos, N., Minikin, A., Ramanathan, V., de Reus, M., Roelofs, G.J., Scheeren, H.A., Sciare, J., Schlager, H., Schultz, M., Siegmund, P., Steil, B., Stephanou, E.G., Stier, P., Traub, M., Warneke, C., Williams, J. and Ziereis, H. (2002). Global air pollution crossroads over the Mediterranean. *Science* 298:794–799.

Li, Z., Niu, F., Fan, J., Liu, Y., Rosenfeld, D. and Ding, Y. (2011). Long-term impacts of aerosols on the vertical development of clouds and precipitation. *Nat. Geosci.* 4: 888–894.

Luo, T., Yuan, R. and Wang, Z. (2014a). Lidar-based remote sensing of atmospheric boundary layer height over land and ocean. *Atmos. Meas. Tech*. 7: 173–182.

Luo, Y., Zheng, X., Zhao, T. and Chen, J. (2014b). A climatology of aerosol optical depth over China from recent 10 years of MODIS remote sensing data. *Int. J. Climatol*. 34: 863–870.

Ma, X. and Yu, F. (2014). Seasonal variability of aerosol vertical profiles over east US and west Europe: GEOS-Chem/APM simulation and comparison with CALIPSO observations. *Atmos. Res.* 140: 28–37.

Martin, R.V. (2008). Satellite remote sensing of surface air quality. *Atmos. Environ.* 42: 7823–7843.

McGrath-Spangler, E.L. and Denning, A.S. (2013). Global seasonal variations of midday planetary boundary layer depth from CALIPSO space-borne LIDAR. *J. Geophys. Res*. 118: 1226–1233.

Menon, S., Hansen, J., Nazarenko, L. and Luo, Y. (2002). Climate effects of black carbon aerosols in China and India. *Science* 297: 2250–2253.

Menut, L., Flamant, C., Pelon, J. and Flamant, P.H. (1999). Urban boundary-layer height determination from lidar measurements over the Paris area. *Appl. Opt*. 38: 945–954.

Omar, A.H., Winker, D.M., Tackett, J.L., Giles, D.M., Kar, J., Liu, Z., Vaughan M.A., Powell K.A. and Trepte, C.R. (2013). CALIOP and AERONET aerosol optical depth comparisons: One size fits none. *J. Geophys. Res*. 118: 4748–4766.

Seinfeld, J.H., Bretherton, C., Carslaw, K.S., Coe, H., DeMott, P.J., Dunlea, E.J., Feingold, G., Ghan, S., Guenther, A.B., Kahn, R., Kraucunas, I., Kreidenweis, S.M., Molina, M.J., Nenes, A., Penner, J.E., Prather, K.A., Ramanathan, V., Ramaswamy, V., Rasch, P.J., Ravishankara, A.R., Rosenfeld, D., Stephens, G. and Wood, R. (2016). Improving our fundamental understanding of the role of aerosol- cloud interactions in the climate system. *Proc. Natl. Acad. Sci. U.S.A.* 113: 5781–5790.

Sheng, N. and Tang, U.W. (2016). The first official city ranking by air quality in China-A review and analysis. *Cities* 51: 139–149.

Stull, R.B. and Eloranta, E.W. (1984). Boundary Layer Experiment 1983. *Bull. Am. Meteorol. Soc*. 65: 450–456.

Sun, K. and Chen, X. (2017) Spatio-temporal distribution of localized aerosol loading in China: A satellite view. *Atmos. Environ.* 163: 35–43.

Sun, L., Xia, X., Wang, P., Zhang, R., Che, H., Deng, Z and Meng, X. (2015). Surface and column-integrated aerosol properties of heavy haze events in January 2013 over the North China Plain. *Aerosol Air Qual. Res.* 15: 1514–1524.

Tao, J., Zhang, L., Gao, J., Wang, H., Chai, F. and Wang, S. (2015). Aerosol chemical composition and light scattering during a winter season in Beijing. *Atmos. Environ.* 110: 36–44.

Tao, J., Zhang, L., Cao, J. and Zhang, R. (2017). A review of current knowledge concerning $PM_{2.5}$ chemical composition, aerosol optical properties and their relationships across China. *Atmos. Chem. Phys.* 17: 9485–9518.

van Donkelaar, A., Martin, R.V. and Park, R.J. (2006). Estimating ground-level $PM_{2.5}$ using aerosol optical depth determined from satellite remote sensing. *J. Geophys. Res*. 111: D21201.

Vernier, J.P., Thomason, L.W. and Kar, J. (2011). CALIPSO detection of an Asian tropopause aerosol layer. *Geophys. Res. Lett*. 38: L07804.

Watson, J. (2002). Visibility: Science and regulation. *J. Air Waste Manage. Assoc.* 52: 628–713.

Winker, D.M., Hunt, B.H. and McGill, M.J. (2007). Initial performance assessment of CALIOP. *Geophys. Res. Lett*. 34: L19803.

Winker, D.M., Vaughan, M.A., Omar, A., Hu, Y., Powell, K.A., Liu, Z., Hunt, W.H. and Young, S.A. (2009). Overview of the CALIPSO mission and CALIOP data processing algorithms. *J. Atmos. Oceanic Technol.* 26: 2310–2323.

Winker, D.M., Pelon, J., Coakley, J.A., Ackerman, S.A.,

Charlson, R.J., Colarco, P.R., Flamant, P., Fu, Q., Hoff, R.M., Kittaka, C., Kubar, T.L., Le Treut, H., McCormick, M.P., Mégie, G., Poole, L., Powell, K., Trepte, C., Vaughan, M.A. and Wielicki, B.A. (2010). The CALIPSO Mission: A global 3D view of aerosols and clouds. *Bull. Amer. Meteor. Soc.* 91: 1211–1230.

Xiao, Q., Wang, Y., Chang, H.H., Meng, X., Geng, G., Lyapustin, A. and Liu, Y. (2017). Full-coverage high-resolution daily $PM_{2.5}$ estimation using MAIAC AOD in the Yangtze River Delta of China. *Remote Sens. Environ.* 199: 437–446.

Yu, H., Chin, M., Winker, D. M., Omar, A.H., Liu, Z., Kittaka, C. and Diehl, T. (2010). Global view of aerosol vertical distributions from CALIPSO lidar measurements and GOCART simulations: Regional and seasonal variations. *J. Geophys. Res*. 115: D00H30.

Yu, L., Wang, G., Zhang, R., Zhang, L., Song, Y., Wu, B. and Chu, J. (2013). Characterization and source apportionment of $PM_{2.5}$ in an urban environment in Beijing. *Aerosol Air Qual. Res*. 13: 574–583.

Yu, W., Liu, Y., Ma, Z. and Bi, J. (2017) Improving satellite-based $PM_{2.5}$ estimates in China using Gaussian processes modeling in a Bayesian hierarchical setting. *Sci. Rep*. 7: 7048.

Zhang, J. and Reid, J.S. (2010). A decadal regional and global trend analysis of the aerosol optical depth using a data-assimilation grade over-water MODIS and Level 2 MISR aerosol products. *Atmos. Chem. Phys*. 10: 10949–10963.

Zhang, W., Guo, J., Miao, Y., Liu, H., Zhang, Y., Li, Z., and Zhai, P. (2016). Planetary boundary layer height from CALIOP compared to radiosonde over China. *Atmos. Chem. Phys*. 16: 9951–9963.

Zhang, X.Y., Wang, Y.Q., Niu, T., Zhang, X.C., Gong, S.L., Zhang, Y.M. and Sun, J.Y. (2012). Atmospheric aerosol compositions in China: Spatial/temporal variability, chemical signature, regional haze distribution and comparisons with global aerosols. *Atmos. Chem. Phys*. 12: 779–799.

Zheng, J., Che, W., Zheng, Z., Chen, L. and Zhong, L. (2013). Analysis of spatial and temporal variability of PM_{10} concentrations using MODIS aerosol optical thickness in the Pearl River Delta Region, China. *Aerosol Air Qual. Res.* 13: 862–876.

Zheng, X., Kang, W., Zhao, T., Luo, Y., Duan, C. and Chen, J. (2008). Long-term trends in sunshine duration over Yunnan-Guizhou Plateau in Southwest China for 1961-2005. *Geophys. Res. Lett.* 35: L15707.

Zheng, X., Wang, X., Luo, Y., Zhao, T. and Chen, J. (2010). The trends and causes of visibility and floating factors during 1961-2006 in Yunnan-Guizhou Plateau. *Ecol. Environ. Sci*. 19: 314–319. (in Chinese)

Received for review, October 15, 2017
Revised, August December 21, 2017
Accepted, January 19, 2018